A Variable Ionized Disk Wind in the Black Hole Candidate EXO 1846–031

Yanan Wang[1,2], Long Ji[3], Javier A. García[4,5], Thomas Dauser[5], Mariano Méndez[6], Junjie Mao[7], L. Tao[8],
Diego Altamirano[2], Pierre Maggi[1], S. N. Zhang[8,9], M. Y. Ge[8], L. Zhang[2], J. L. Qu[8,9], S. Zhang[8], X. Ma[8], F. J. Lu[8],
T. P. Li[8,9,10], Y. Huang[8], S. J. Zheng[8], Z. Chang[8], Y. L. Tuo[8,9], L. M. Song[8,9], Y. P. Xu[8], Y. Chen[8], C. Z. Liu[8], Q. C. Bu[8],
C. Cai[8], X. L. Cao[8], L. Chen[11], T. X. Chen[8], Y. P. Chen[8], W. W. Cui[8], Y. Y. Du[8], G. H. Gao[8,9], Y. D. Gu[8], J. Guan[8], C. C. Guo[8,9],
D. W. Han[8], J. Huo[8], S. M. Jia[8], W. C. Jiang[8], J. Jin[8], L. D. Kong[8,9], B. Li[8], C. K. Li[8], G. Li[8], W. Li[8], X. Li[8], X. B. Li[8],
X. F. Li[8], Z. W. Li[8], X. H. Liang[8], J. Y. Liao[8], H. W. Liu[8], X. J. Liu[8], X. F. Lu[8], Q. Luo[8,9], T. Luo[8], B. Meng[8], Y. Nang[8,9],
J. Y. Nie[8], G. Ou[8], N. Sai[8,9], R. C. Shang[10], X. Y. Song[8], L. Sun[8], Y. Tan[8], W. S. Wang[8], Y. D. Wang[11], Y. S. Wang[8], X. Y. Wen[8],
B. B. Wu[8], B. Y. Wu[8,9], M. Wu[8], G. C. Xiao[8,9], S. Xiao[8,9], S. L. Xiong[8], S. Yang[8], Y. J. Yang[8], Q. B. Yi[8,9], Q. Q. Yin[8], Y. You[8],
F. Zhang[8], H. M. Zhang[8], J. Zhang[8], W. C. Zhang[8], W. Zhang[8,9], Y. F. Zhang[8], H. S. Zhao[8], X. F. Zhao[8,9], and D. K. Zhou[8,9]

[1] Université de Strasbourg, CNRS, Observatoire astronomique de Strasbourg, UMR 7550, F-67000 Strasbourg, France; yanan.wang@astro.unistra.fr
[2] Physics & Astronomy, University of Southampton, Southampton, Hampshire SO17 1BJ, UK
[3] Institut für Astronomie und Astrophysik, Kepler Center for Astro and Particle Physics, Eberhard Karls Universität, Sand 1, D-72076 Tübingen, Germany
[4] Cahill Center for Astronomy and Astrophysics, California Institute of Technology, Pasadena, CA 91125, USA
[5] Dr Karl Remeis-Observatory and Erlangen Centre for Astroparticle Physics, Sternwartstr. 7, D-96049 Bamberg, Germany
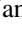[6] Kapteyn Astronomical Institute, University of Groningen, PO Box 800, 9700 AV Groningen, The Netherlands
[7] Department of Physics, University of Strathclyde, Glasgow G4 0NG, UK
[8] Key Laboratory for Particle Astrophysics, Institute of High Energy Physics, Chinese Academy of Sciences, 19B Yuquan Road, Beijing 100049,
People's Republic of China
[9] University of Chinese Academy of Sciences, Chinese Academy of Sciences, Beijing 100049, People's Republic of China
[10] Department of Astronomy, Tsinghua University, Beijing 100084, People's Republic of China
[11] Department of Astronomy, Beijing Normal University, Beijing 100088, People's Republic of China

Abstract

After 34 yr, the black hole candidate EXO 1846–031 went into outburst again in 2019. We investigate its spectral properties in the hard intermediate and the soft states with NuSTAR and Insight-HXMT. A reflection component has been detected in the two spectral states but possibly originating from different illumination spectra: in the intermediate state, the illuminating source is attributed to a hard coronal component, which has been commonly observed in other X-ray binaries, whereas in the soft state, the reflection is probably produced by disk self-irradiation. Both cases support EXO 1846–031 as a low-inclination system of $\sim40°$. An absorption line is clearly detected at ~7.2 keV in the hard intermediate state, corresponding to a highly ionized disk wind ($\log \xi > 6.1$) with a velocity of up to $0.06c$. Meanwhile, quasi-simultaneous radio emissions have been detected before and after the X-rays, implying the coexistence of disk winds and jets in this system. If only the high-flux segment of the NuSTAR observation is considered, the observed wind appears to be magnetically driven. The absorption line disappeared in the soft state and a narrow emission line appeared at ~6.7 keV on top of the reflection component, which may be evidence for disk winds, but data with higher spectral resolution are required to examine this.

Unified Astronomy Thesaurus concepts: High energy astrophysics (739); X-ray transient sources (1852); Accretion (14)

1. Introduction

Low-mass X-ray binaries (LMXBs) harbor a compact object, either a neutron star or a black hole, and a companion star with mass smaller than or similar to that of the Sun (e.g., Frank et al. 2002). X-ray transients spend most of their lives in a quiescent state but show bright outbursts lasting for weeks to months with a recurrence time varying from months to decades (Tanaka & Shibazaki 1996; Chen et al. 1997; Tomsick & Kaaret 2000). Compared to supermassive black holes, stellar-mass black holes display much richer and faster variability and thus provide an ideal window to study the evolution of extreme astrophysical phenomena, such as accretion and ejection processes, in an observable timescale (e.g., Shakura & Sunyaev 1973; Poutanen & Fabian 1999; Belloni et al. 2000; Uttley et al. 2005, 2014; Altamirano & Méndez 2015; Wang et al. 2020).

A typical outburst starts with a rapid increase of the source luminosity by several orders of magnitude, and then the luminosity decreases over a much longer time period. Along with such an outburst, black hole X-ray binaries (BHXBs) exhibit different characteristics in their spectra and fluxes (e.g., Miyamoto et al. 1991; van der Klis 1995; Méndez & van der Klis 1997; Remillard & McClintock 2006). Two main spectral states, soft and hard, have been generally distinguished in a complete cycle of an outburst. In the soft state, the spectrum shows prominent thermal emission from an accretion disk. In the hard state, the spectrum is dominated by nonthermal emission from a hot corona or the base of a jet (e.g., Markoff et al. 2005), where the soft photons from an accretion disk are inversely Compton scattered by the hot electrons of the corona. Additionally, an intermediate state occurs when the source transitions between these two states.

Apart from the thermal and nonthermal components, emission- and absorption-line features have also been widely observed in BHXBs, especially the broad emission line centered at 6.4–7 keV (e.g., Laor 1991; Miller 2007; García et al. 2015; Wang et al. 2018). As the most prominent feature of disk reflection, such emission line is produced when the nonthermal/hard emission illuminates the accretion disk (Lightman & White 1988;

George & Fabian 1991; García et al. 2014; Dauser et al. 2014), though the illuminating source has also been attributed to the surface emission or the boundary layer in neutron star X-ray binaries (e.g., Ross & Fabian 2005; Cackett et al. 2010; Miller et al. 2015; Wang et al. 2019). Most recently, Connors et al. (2020) found one intriguing case in which the disk reflection in the very soft state in the BHXB XTE J1550–564 was produced by self-irradiation of the innermost part of the accretion disk.

With regard to the absorption lines discovered in BHXBs, the highly ionized ones have been attributed to the presence of disk winds, which have been suggested to be responsible for the quenching of jets (e.g., Miller et al. 2008; Neilsen & Lee 2009). Such line features, for instance, Fe XXV and Fe XXVI absorption lines, are preferentially observed in systems with high inclination angles in the soft state (Ponti et al. 2012), e.g., 4U 1630–472 (Díaz Trigo et al. 2014; Miller et al. 2015), GRO J1655−40 (Miller et al. 2006a, 2008), H 1743–322 (Miller et al. 2006b, 2012), and GRS 1915+105 (Neilsen & Lee 2009; Ueda et al. 2009). Theoretical studies show that such lines could be driven by radiation pressure, thermal or magnetic forces, or even the combination of these (e.g., Proga & Kallman 2002; Tomaru et al. 2019). However, the driving mechanism is still debated in accreting systems.

EXO 1846–031 was discovered on 1985 April 3; it was suggested that the source is a black hole candidate (BHC) due to its ultrasoft spectral component observed with EXOSAT (Parmar et al. 1993). After 34 yr of quiescence, the Monitor of All-sky X-ray Image (MAXI/GSC) observed EXO 1846–031 being active from 2019 July 23. A low-frequency quasi-periodic oscillation (QPO) at 0.71 ± 0.01 Hz in the energy band 25–250 keV has been observed with the Hard X-ray Modulation Telescope (HXMT), dubbed Insight-HXMT, in the hard state (Yang et al. 2019). The QPO frequency increases with the source luminosity, which is a typical phenomenon observed in BHXBs. Besides that, disk reflection and disk winds have been observed in one Nuclear Spectroscopic Telescope Array (NuSTAR; Harrison et al. 2013) spectrum of this source (Miller et al. 2019). These authors report an outflowing velocity of $0.01c$ of the absorbing gas.

In this work, we examine the observed absorption feature with the NuSTAR observation of EXO 1846–031 in the hard intermediate state with a self-consistent photoionization model and explore its driving mechanism. We then further investigate how the outflow observed in the intermediate state behaves in the following soft state with an Insight-HXMT observation. Finally, we discuss the origin of the absorption and emission lines in EXO 1846–031.

2. Observations and Data Analysis

The Neil Gehrels Swift Observatory (Swift; Gehrels et al. 2004) and NuSTAR observed the outburst of EXO 1846–031 on 2019 August 2 and 3. Insight-HXMT observed the source on 2019 September 15 (we will use HXMT, short for Insight-HXMT, in the rest of this paper). More details about the observations are shown in Table 1.

The Swift/XRT data were taken in the Windowed Timing mode. We reduced the data using XRTPIPELINE following the official user's guide.[12] Using the NuSTAR Data Analysis Software (NuSTARDAS v2.0.0), we created the NuSTAR spectra and lightcurves of the source and the background with

---
[12] https://swift.gsfc.nasa.gov/analysis/xrt_swguide_v1_2.pdf

Table 1
Swift, NuSTAR, and HXMT Observations of EXO 1846–031 Used in This Paper

Mission/Instrument	ObsID	MJD	Exposure (ks)
Swift/XRT	00011500002	58697.3	1.1
NuSTAR/FPMA	90501334002	58698.1	22.2
NuSTAR/FPMB			22.6
HXMT/LE	P0214050022	58741.1	13.8
HXMT/ME			24.6

two circular extraction regions of $80''$, one centered at the source and another one centered away from the source. NuSTAR CALDB (v20200912) is applied in this work.

We extracted the HXMT lightcurves and spectra by following the official user guide[13] and using the latest software HXMTDAS (v2.02; Zhang et al. 2020). The criteria for screening good time intervals are as follows: (1) elevation angle $>10°$, (2) geomagnetic cutoff rigidity >8 GeV, (3) pointing offset angle $<0°.1$, and (4) at least 300 s away from the South Atlantic Anomaly (SAA). The background was estimated using the scripts LEBKGMAP and MEBKGMAP (Liao et al. 2020; Guo et al. 2020). The energy bands used in the spectral analysis are 1–9 keV and 10–20 keV for the low- and medium-energy (LE and ME) detectors, respectively (Chen et al. 2020; Cao et al. 2020).

The spectra were grouped into bins to have at least 30 counts (Cash 1979). To account for the neutral hydrogen column absorption of the interstellar medium, we employed the tbabs model and the WILM solar abundance (Wilms et al. 2000) in xspec (v12.11.1). In this paper, all uncertainties are quoted at the 1σ confidence level.

3. Analysis and Results

Figure 1 shows the long-term lightcurves in the 2–10 keV and 15–50 keV bands observed with MAXI and Swift/BAT in red and black, respectively. It is clear that the peak of hard X-rays precedes that of soft X-rays, showing the canonical evolution of outbursts in LMXBs (e.g., Remillard & McClintock 2006; Belloni 2010; Muñoz-Darias et al. 2011). Liu et al. (2020) conducted a timing analysis of EXO 1846–031 in the same outburst with HXMT and the Neutron star Interior Composition Explorer (NICER). Based on the relative changes in the hardness ratio diagram and the fractional rms integrated in 2^{-5}–32 Hz, they classify the entire outburst into four spectral states, i.e., low hard, hard intermediate, soft intermediate, and high soft (see the gray dashed lines in Figure 1). According to their classification, our Swift/XRT and NuSTAR observations took place in the hard intermediate state and the HXMT observation took place in the soft state. Although it is unclear when the source left the soft state in the end because of the low count rate, this does not affect the results present in this paper.

We extracted the NuSTAR background-subtracted lightcurves in the 3–10 keV and 10–79 keV energy bands (Figure 2) and calculated the hardness ratio. It is clearly shown that the count rate (the summation of FPMA and FPMB) gradually increases with time by around 10%, accompanied by a reduction of the hardness, i.e., a spectral softening. We hence separated the NuSTAR spectrum into two segments with similar counts, low flux and high

---
[13] http://enghxmt.ihep.ac.cn/sjfxwd/169.jhtml
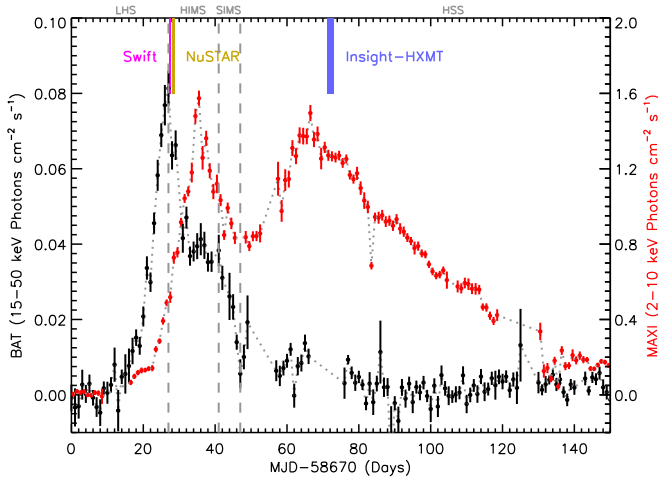
Figure 1. Long-term lightcurves of EXO 1846–031 during its 2019 outburst observed with Swift/BAT (15–50 keV, black points) and MAXI (2–10 keV, red points). The magenta, yellow, and blue bars represent the time of the Swift, NuSTAR, and HXMT observations. The gray dashed lines indicate the spectral states of EXO 1846–031, taken from Liu et al. (2020). "LHS," "HIMS," "SIMS," and "HSS" are short for low hard, hard intermediate, soft intermediate and high soft states, respectively.
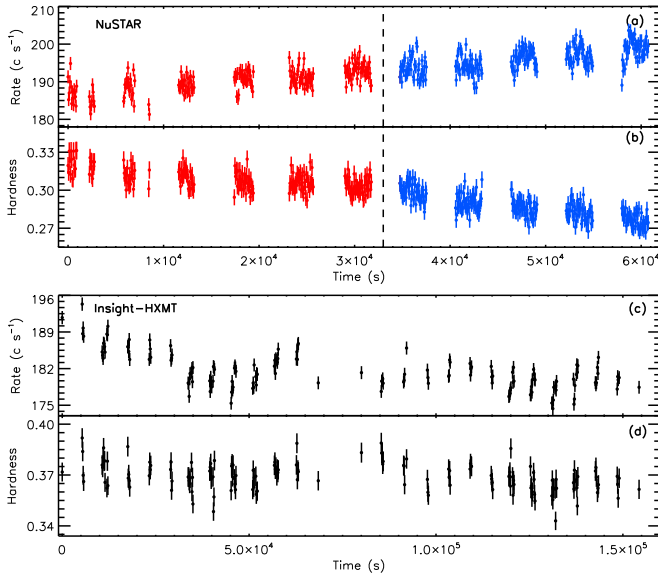
Figure 2. Upper panels: the count rate of both modules in the 3–79 keV band and the hardness ratio (10–79 keV/3–10 keV) during the NuSTAR observation of EXO 1846–031. The dashed line separates the observation into low-flux (red) and high-flux (blue) segments. Lower panels: the count rate in the 1–10 keV band and the hardness ratio (4–10 keV/1–4 keV) during the HXMT observation.

flux, as the dashed line in Figure 2 indicates. As to the background-subtracted HXMT lightcurve, the hardness ratio between the lightcurves in the 4–10 keV and 1–4 keV bands shows no clear trend with time (see the bottom panel of Figure 2). We thus conduct a time-average spectral analysis with the HXMT observation.
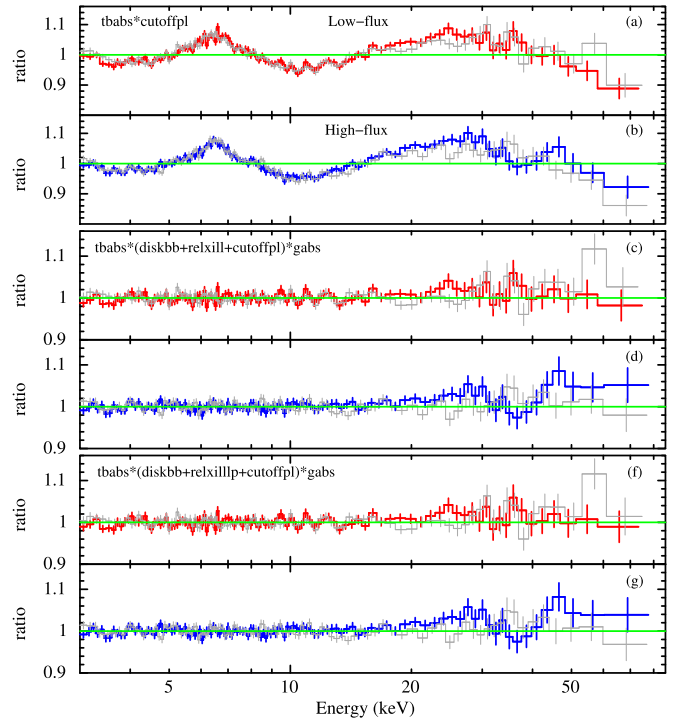
3.1. Spectral Analysis

Because the Swift, NuSTAR and HXMT observations caught EXO 1846–031 in different spectral states, we analyzed them separately and applied different models to fit the spectra with individual requirements.

Figure 3. Ratio residuals of the 3–78 keV NuSTAR spectra of EXO 1846–031 to different models. The red and blue lines represent the FPMA spectra in the low and high flux, respectively. The FPMB spectra are shown in gray for reference.

3.1.1. The Hard-component-dominated State

We fitted the Swift/XRT spectrum with an absorbed power law, `tbabs*powerlaw`, in the energy band 1–10 keV and obtained a column density, $N_H = 6 \pm 0.1 \times 10^{22}$ cm^{-3}, a photon index, $\Gamma = 1.55 \pm 0.03$ and the normalization of the component `powerlaw`, 1.0 ± 0.1, with $\chi^2 = 615.5$ for 588 degrees of freedom (dof). Adding a soft component, `diskbb`, to the model improves the fit by $\Delta\chi^2 = 5.32$ for 2 dof fewer whereas the F-test probability of 0.08 indicates that this component is not significantly required by the data.

We jointly fitted the 3–79 keV FPMA and B continuum of the two segments of the NuSTAR observation with an absorbed power law with a high-energy cutoff `cutoffpl`. We fixed the value of the column density at the one derived from the fit to the XRT spectrum, $N_H = 6 \times 10^{22}$ cm^{-3}, and obtained a fit with $\chi^2 = 8746.8$ for 4149 dof. Figures 3(a) and b show the ratio residuals of the spectra to the continuum model `tbabs*cutoffpl`. The residuals show a broad emission line centered at 6–7 keV and a hump peaking at 20–30 keV, indicating the presence of a reflection spectrum. We thus continued our spectral analysis by including physical reflection models `relxill(lp)` (v1.3.9[14]) in which the reflection component is produced by the irradiation of the hard component.

In both models, `relxill` and `relxilllp`, we adopted the outer radius, $R_{out} = 400\,R_g$ ($R_g = GM/c^2$). We assumed that the spin parameter, a_*, the inclination of the system, i, and the iron abundance, A_{Fe}, of the accretion disk do not vary on the timescales of the observation and hence we linked these parameters during the fit to be the same in the two segments.

---

[14] http://www.sternwarte.uni-erlangen.de/~dauser/research/relxill/
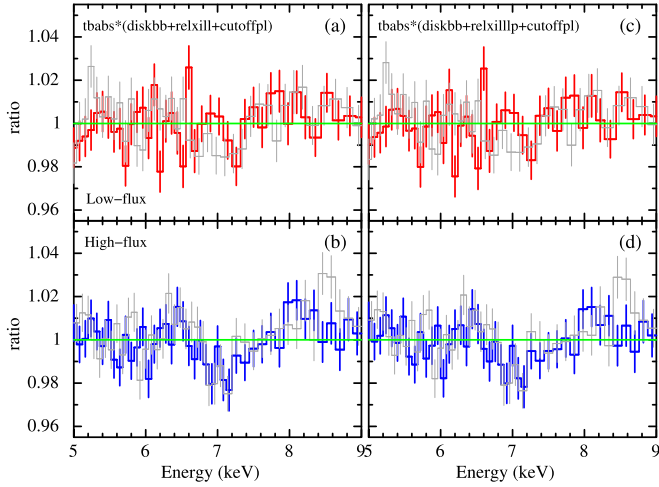
Figure 4. Ratio residuals of the 5–9 keV NuSTAR spectra of EXO 1846–031 to different models. The colors are defined the same as in Figure 3.

We linked the outer emissivity index to the inner one, $q_{out} = q_{in}$, to vary together in relxill. Compared to relxill, relxilllp assumes a lamppost geometry for the illuminating source. When we fitted this component, the spin parameter could not be constrained by the data. We thus fixed it at the upper limit, i.e., $a_* = 0.998$, allowing the maximum space parameter for the disk inner radius.

We got a reasonably good fit by including the reflection component; e.g., in the fit using relxill, the best fit is $\chi^2 = 4329.2$ for 4132 dof. Meanwhile, there is a soft excess present below 5 keV. Adding the component diskbb to the model improves the fit with $\Delta\chi^2 = 103.8$ for 4 dof fewer. We therefore include this component in our model.

Additionally, a moderately broad absorption feature appears in the spectra (see Figure 4). In both segments, the absorption feature is independent of the choice of the reflection model. For the high-flux segment, the strength of the absorption feature is consistent in both the FPMA and B spectra, whereas for the low-flux segment, the feature in the FPMA spectrum is subtle. To test if an absorption line is required in the fit of the low-flux segment, we added an absorption-line component, gabs, at ~7.2 keV to the model. The component gabs cannot be well constrained if we let its parameters vary between the FPMA and B spectra. We hence linked the parameters of gabs between the two spectra. The fit to the low-flux spectra improved by $\Delta\chi^2 = 32.1$ for 3 dof fewer. We thus included gabs in our model and the overall fit to the four spectra significantly improved, for instance, $\Delta\chi^2 = 103.3$ for 6 dof fewer in the fit with relxill. We obtained the best-fitting reflection fraction, for the low- and high-flux segments, of 0.10 ± 0.01 and 0.11 ± 0.01 in relxill and 0.26 ± 0.04 and 0.29 ± 0.02 in relxilllp, respectively. In order to calculate the individual flux of the reflection and the power law, we set the reflection fraction to a negative value, which makes relxill and relxilllp only account for the reflection component.

We show the best-fitting parameters and the individual fluxes, F_{dbb}, F_{rel}, F_{pl}, and total flux, F_{tt}, in Table 2. Ratio plots of the models are shown in Figure 3. The fits of the model with either relxill or relxilllp are equally good, and the parameters common in both models are consistent. The inclination angle of the accretion disk ranges from 37° to 44° and the iron abundance is about 5 in units of solar abundance. The inner radius of the

accretion disk is weakly constrained, $R_{in} = 1 - 11\,R_g$, in the low-flux segment and $R_{in} = 1 - 84\,R_g$ in the high-flux segment. The photon index slightly increases as the total flux increases. Additionally, the large coronal height provided by the component relxilllp probably explains why the spin of this source is hard to constrain (Dauser et al. 2013; Fabian et al. 2014).

Miller et al. (2019) have reported the presence of an absorption line in EXO 1846–031 as well as a higher inclination angle, 75°, than ours. To check if we have obtained the inclination angle at a clear global minimum and to assess a possible correction between the absorption line and the inclination, we plotted χ^2 confidence contours between the inclination and the line energy or width of the gabs component. Figure 5 shows that although the disk inclination is correlated to the energy of the gabs, the inclination angle is independent of the width of the gabs and is lower than 45° at 90% confidence level. If we freeze the inclination angle at 75°, the fit worsens with $\Delta\chi^2 = 26.5$ for 1 dof fewer. We provide further comparison at the end of Section 4.1.

To explore the physical properties of the absorbing gas which produces the absorption features, we created a grid of photoionization models with XSTAR (Kallman & Bautista 2001) using a power-law spectral input form with $\Gamma = 1.8$ based on the fit to the NuSTAR observation. For the other parameters of this grid of models, we set fixed values of a gas density at $n_{gas} = 10^{15}\,cm^{-3}$ and a covering fraction at $f = \Omega/4\pi = 0.5$, following the assumptions for disk winds in LMXBs (Miller et al. 2015), a source luminosity at $L = 2.2 \times 10^{38}\,erg\,s^{-1}$ in the energy band 0.01–100 keV (a distance of 8 kpc is adopted from Miller-Jones et al. 2019). We calculated the turbulent velocity of the outflow with the best-fitting energy and width of gabs and obtained $v_{turb} = 7000 \pm 4100\,km\,s^{-1}$ for the low-flux segment and $v_{turb} = 13,000 \pm 1700\,km\,s^{-1}$ for the high-flux segment. We hence adopted an average turbulent velocity of $10,000\,km\,s^{-1}$ as the input. The variable parameters are the iron abundance, A_{Fe}, the equivalent hydrogen column density, N_{gas}, ionization parameter, ξ_{gas}, and the shift velocity, v. The grid was read into XSPEC as a multiplicative model to fit the NuSTAR spectra, replacing the line model gabs, in which the iron abundance in the grid photoionization model was linked to that in the reflection model.

The absorption feature is well fit with the precalculated grid. We show the best-fitting parameters of the grid in Table 3. The rest of the parameters obtained here are consistent with those obtained from the fit with gabs. The measured parameters of the low-flux segment are not constrained as well as those of the high-flux, but both suggest a highly ionized and fast outflowing wind in EXO 1846–031.

Once the ionization parameter is obtained, we can use it to calculate the launching radius of the disk winds and the mass outflow rate. We define the launching radius of disk winds as $R_{launch} = \sqrt{L/n_{gas}\xi_{gas}}$, where L is the ionizing luminosity, n_{gas} is the gas density, and ξ_{gas} is the ionization parameter (Tarter et al. 1969; Kallman & Bautista 2001). Regarding the wind mass outflow rate, we estimated it through $\dot{M}_{wind} = \Omega\mu m_p v L/\xi_{gas}$, where Ω is the opening angle ($\Omega = 2\pi$ is assumed), μ is the average molecular weight of the gas ($\mu = 1.23$ is assumed as in some other black hole systems; e.g., Janiuk et al. 2015; Trueba et al. 2019), m_p is the mass of a proton, and v is the outflow velocity. The mass accretion rate is roughly estimated as $\dot{M}_{acc} = L/(\eta c^2)$, where the efficiency $\eta = 0.1$ is assumed. The calculated launching radius and the ratio of the mass outflow rate

Table 2
Best-fitting Parameters of the Two NuSTAR Segments of EXO 1846–031 with the Models `tbabs*(diskbb+relxill+cutoffpl)*gabs` and `tbabs*(diskbb+relxilllp+cutoffpl)*gabs` in the Energy Band 3–79 keV

Components		relxill		relxilllp	
		Low Flux	High Flux	Low Flux	High Flux
`tbabs`	$N_{\rm H}$ (10^{22} cm^{-2})	6.0^f		6.0^f	
`diskbb`	$T_{\rm dbb}$ (keV)	0.40 ± 0.04	0.52 ± 0.05	0.41 ± 0.04	0.52 ± 0.06
	$N_{\rm dbb}$ ($R_{\rm dbb}^2/D_{10}^2 \cos i$)	$11849.7^{+18985}_{-6830.4}$	$1772.2^{+1961.5}_{-819.8}$	$9816.9^{+17516.2}_{-5478.3}$	$1582.6^{+1522.9}_{-779.1}$
`relxill(lp)`	$q_{\rm in}$	2.6 ± 0.4	1.9 ± 0.3	...	...
	h ($R_{\rm g}$)	...	...	10.2 ± 5.2	$21.0^{+478.4}_{-19.0}$
	$A_{\rm Fe}$ ($A_{\rm Fe\odot}$)	5.0 ± 0.6^l		5.0 ± 0.5^l	
	i ($^\circ$)	$41.4^{+2.6}_{-1.5}$		$38.8^{+1.6l}_{-2.2}$	
	a_*	0.998^f		0.998^f	
	Γ	1.75 ± 0.01	1.81 ± 0.01	1.76 ± 0.01	1.82 ± 0.01
	$E_{\rm cut}$ (keV)	$62.5^{+2.5}_{-2.0}$	63.2 ± 2.6	$62.0^{+2.4}_{-3.5}$	$65.8^{+2.5}_{-1.3}$
	Refl_frac	-1^f	-1^f	-1^f	-1^f
	$R_{\rm in}$ ($R_{\rm g}$)	$3.1^{+2.7}_{1p}$	$1.8^{+19.0}_{1p}$	$3.3^{+7.8}_{1p}$	$59.5^{+24.8}_{-17.9}$
	$\log \xi$ (erg cm s^{-1})	$3.71^{+0.04}_{-0.12}$	3.82 ± 0.05	$3.72^{+0.03}_{-0.11}$	3.91 ± 0.05
	$N_{\rm rel(lp)}$ (10^{-3})	2.0 ± 0.2	2.2 ± 0.2	8.2 ± 1.5	$6.7^{+3.4}_{-1.1}$
`cutoffpl`	$N_{\rm pl}$	1.2 ± 0.1	1.3 ± 0.1	1.2 ± 0.1	1.3 ± 0.1
`gabs`	$E_{\rm gabs}$ (keV)	7.25 ± 0.05	7.24 ± 0.05	7.24 ± 0.04	7.23 ± 0.05
	$\sigma_{\rm gabs}$ (keV)	0.17 ± 0.10	0.31 ± 0.04	0.17 ± 0.09	0.37 ± 0.07
	strength (10^{-2})	2.0 ± 0.6	3.6 ± 0.6	2.0 ± 0.4	4.1 ± 1.0
`const`	FPMA	1^f		1^f	
	FPMB	1.003 ± 0.001		1.003 ± 0.001	
χ^2/d.o.f.		4122.2/4122		4124.7/4122	
	$F_{\rm dbb}$	0.4 ± 0.1	0.4 ± 0.1	0.4 ± 0.1	0.4 ± 0.1
	$F_{\rm rel}$	1.2 ± 0.1	1.6 ± 0.2	1.2 ± 0.1	1.6 ± 0.1
	$F_{\rm pl}$	4.2 ± 0.1	4.2 ± 0.2	4.2 ± 0.1	4.2 ± 0.1
	$F_{\rm tt}$	5.9 ± 0.1	6.2 ± 0.1	5.8 ± 0.1	6.2 ± 0.1

Note: The first and the second groups are corresponding to the fits with `relxill` and `relxilllp`, respectively. The symbol l indicates that the parameters are linked to vary across the observations; p means that the parameter pegs at its limit; f means that the parameter is fixed during the fit. All of the unabsorbed fluxes, $F_{\rm dbb}$, $F_{\rm rel}$, $F_{\rm pl}$ and $F_{\rm tt}$, are calculated in the energy band of $2-10$ keV in units of 10^{-9} erg cm^{-2}s^{-1}.

over the mass accretion rate are also listed in Table 3. Overall, all the parameters of the photoionization model of the two segments are consistent within errors.

3.1.2. The Soft-component-dominated State

For the HXMT observation, we jointly fitted the continuum of the LE and ME spectra in the energy bands 2–9 keV and 10–20 keV with the model `tbabs*(diskbb+cutoffpl)`. This gives a fit with $\chi^2 = 1053.6$ for 991 dof. Surprisingly, the spectrum in the soft state does not show the need for an absorption line like the source in the intermediate state, but it requires a narrow emission line around 6.7 keV (see the residuals in Figure 6(a)). Besides that, there seems to be a weak excess appearing at above 10 keV.
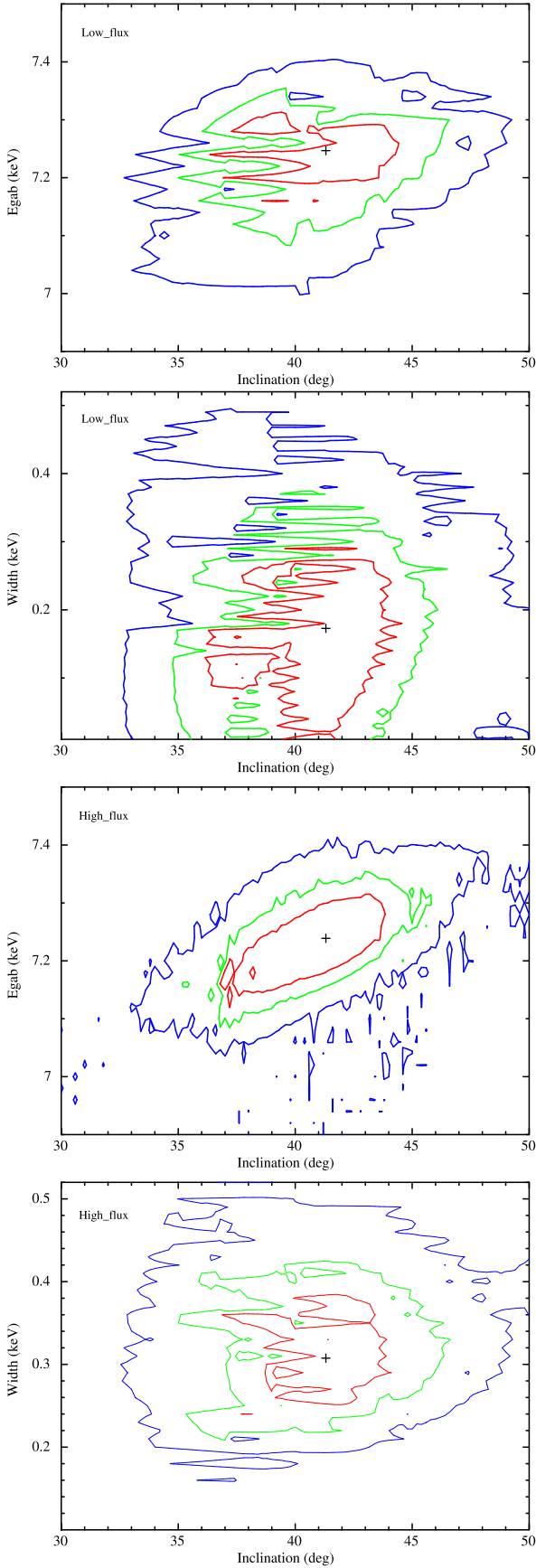
Both features, an emission line at ~6.7 keV and an excess at above 10 keV, hint at the presence of a reflection spectrum. After adding the reflection component `relxill` to the model, the fit improved with $\Delta\chi^2 = 76.9$ for 6 dof fewer. However, Figure 6(b) shows that the emission feature still appears. We hence added a `Gaussian` component to account for this feature which improves the spectral fit by $\Delta\chi^2 = 40.5$ for 3 dof fewer. The overall model is `tbabs*(diskbb+Gaussian+relxill+cutoffpl)`. Here, `relxill` only accounts for the reflection spectrum when a negative reflection fraction is adopted. We show

the individual component in Figure 7(a) and the best-fitting parameters, as well as the individual flux of each component, in Table 4.
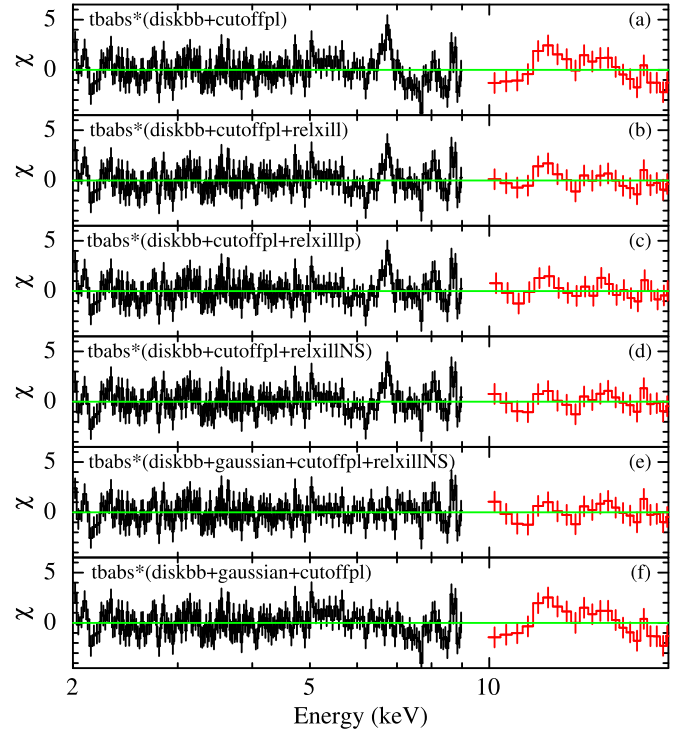
The disk temperature obtained from the fit to the HXMT spectra is 0.94 ± 0.01 keV. The inner radius of the accretion disk is between $2.7 - 4.1\ R_{\rm g}$. Compared to the intermediate state, the higher `diskbb` temperature, higher photon index, and smaller inner radius are consistent with the fact that the source evolves to the soft state. However, the hard component in this model is somehow negligible: adding this component has no effect on the fit. This result seems very odd that a reflection spectrum exists without an illuminating source, i.e., a hard coronal component in this case.

We then replaced the reflection component `relxill` with its lamppost version `relxilllp` to fit the HXMT spectra. Again, the narrow emission line at ~6.7 keV appears on top of the broad line (see Figure 6(c)). After adding a `Gaussian` component, the best-fitting parameters in both models are consistent (see the relevant results in Figures 6 and 7 and Table 4). Similar to the result with `relxill`, the hard component in `relxilllp` is also negligible.

We use the ratio $R_{\rm s}$ to parameterize the strength of the reflection as a ratio of the fluxes of the reflection component to that of the incident continuum in a selected energy band, as

Figure 6. Residuals of the HXMT spectra to different models. The black and red lines represent the LE and ME spectra, respectively.
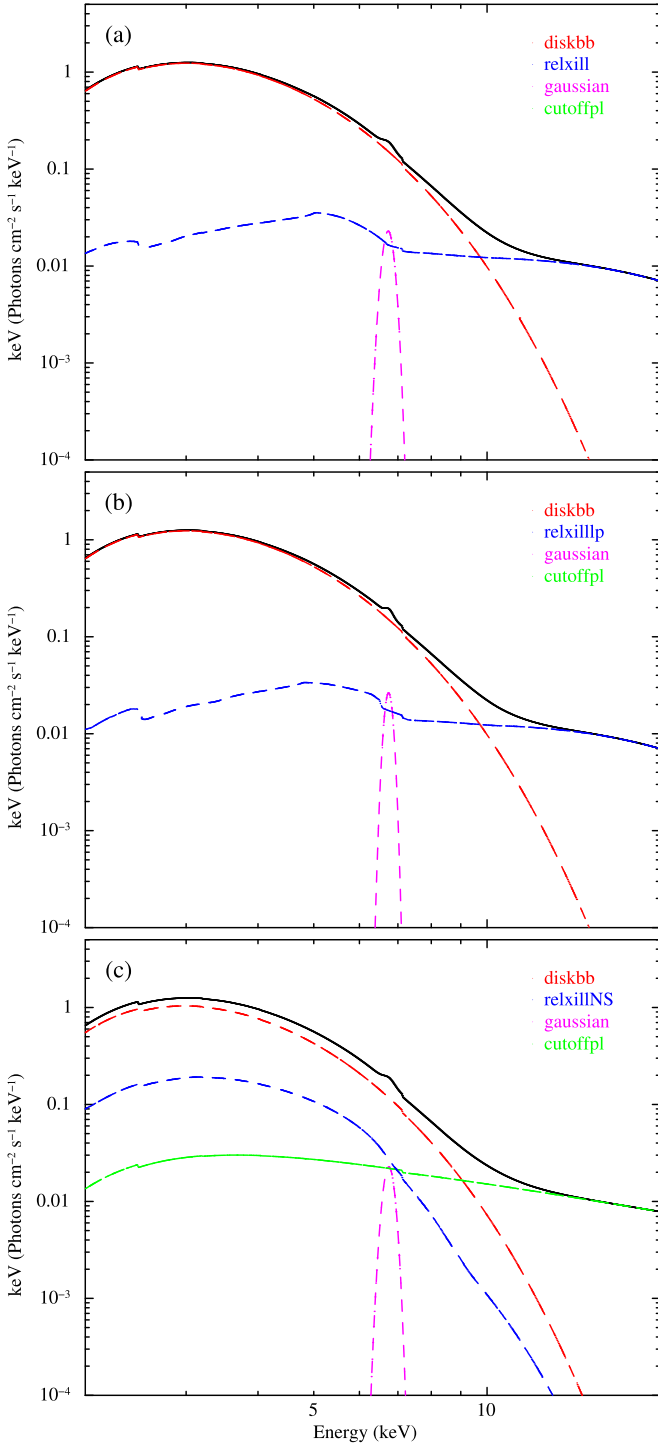
Table 3
The Assumed Input and Measured Output Parameters of the XSTAR Model Applied to the NuSTAR Segments and the Derived Wind Properties in EXO 1846–031

	xstar	Low Flux	High Flux
Input	Γ	-1.8	
	L (10^{38} erg s^{-1})	2.2	
	$\log n_{gas}$ (cm^{-3})	15	
	$f = \Omega/4\pi$	0.5	
	v_{turb} (km s^{-1})	10000	
Output	N_{gas} (10^{22} cm^{-2})	$1.61^{+1.79}_{-0.17}$	$1.71^{+0.09}_{-0.15}$
	$\log \xi_{gas}$ (erg cm s^{-1})	$6.40^{+0.96}_{-0.15}$	6.23 ± 0.04
	v/c	-0.05 ± 0.02	-0.06 ± 0.01
Measurement	R_{launch} (10^{10} cm)	0.03 ± 0.02	0.04 ± 0.002
	$\dot{M}_{wind}$ (10^{18} g s^{-1})	$1.70^{+3.75}_{-0.59}$	3.01 ± 0.28
	$\dot{M}_{wind}/\dot{M}_{acc}$	$0.69^{+1.53}_{-0.24}$	1.23 ± 0.11

used by, e.g., Tao et al. (2015) and Dauser et al. (2016). We calculate R_s in the 10–20 keV band: for the case of relxill, $R_s \approx 2 \times 10^8$, and for the case of relxilllp, $R_s \approx 5 \times 10^8$. Dauser et al. (2016) report that the reflection strength is strongly dependent on the disk inclination angle and the coronal height if a lamppost geometry is assumed. Nevertheless, for no configuration is such a high reflection strength expected.

Inspired by the work of Connors et al. (2020), a reflection spectrum can be produced by disk self-irradiation when the source is in a very soft state. While the inner accretion disk approaches the inner stable circular orbit (ISCO), the gravitational pull of the black hole could bend the thermal photons

Figure 5. Contour plots for the energy or the width of the absorption line vs. disk inclination at the 68% (red), 90% (green), and 99% (blue) confidence levels. The best-fitting values of these parameters are marked with a cross.

Figure 7. Individual components in the fit to the HXMT spectra of EXO 1846–031 in the 2–20 keV. The component `cutoffpl` in the first two figures is negligible.

back and illuminate itself. The model, `relxillNS` (T. Dauser & J. García 2020, in preparation), was originally designed for the reflection originating from the accretion disk in a neutron star system, in which the illuminating source is a single-temperature blackbody. As in Connors et al. (2020), we fixed the inner radius in `relxillNS` at the ISCO, where the `diskbb` temperature is assumed to be sufficient enough to illuminate the disk. The electron density and the iron abundance of the accretion disk are degenerate and always

pegs at their upper limits; we thus fixed the electron density, $\log(n_{\rm e}/{\rm cm}^{-3}) = 19$, and allowed the iron abundance to vary.

We show the result of the fit with `relxillNS` in Figures 6 and 7 and Table 4. The inclination angle and iron abundance are consistent with the values obtained in the intermediate state. Besides that, the photon index derived from `relxillNS` is 1.97 ± 0.09, much lower than the ones derived from `relxill` and `relxilllp`.

If we do not include any reflection component in the model (see the residuals in Figure 6(f)), the fit becomes significantly worse, $\Delta\chi^2 = 75.1$ for 7 dof more, with associated F-test probability $\sim 1 \times 10^{-13}$. In this step, we fixed the centroid energy and the width of Gaussian at their best-fitting values, i.e., $E_{\rm gau} = 6.75$ keV and $\sigma_{\rm gau} = 0.14$ keV, to avoid affecting other features. Figure 6(f) shows that besides the high-energy hump, there is a slight excess centered at 5–6 keV. Adding a single blackbody component, `bbody` in XSPEC, we obtained a fit with $\chi^2 = 965.2$ for 988 dof, which is worse than the fit with `relxillNS` with $\Delta\chi^2 = 21.2$ for 5 dof more. Meanwhile, the best-fitting photon index increases to $5.56^{+1.71}_{-0.53}$, which makes this case less convincing.

Figures 6(b), (c), and (d) show that the residual feature at ~ 6.7 keV is independent of the choice of the reflection component. We calculated the line significance by simulating 1000 spectra using the XSPEC script `simftest` in which the centroid energy of the Gaussian component is allowed to vary within its 1σ confidence region. Based on the model with `relxillNS`, the observed change in χ^2 is 37.9, and the probability of finding such a change by chance is 1.1×10^{-21}, which corresponds to 9.5σ significance.

To better understand the nature of this narrow emission line, we tested two possibilities here. We first tried the possibility of a distant reflector, fitting the line with an unblurred reflection component `xillver`. We linked all of the parameters in `xillver` to those in `relxillNS` except for the ionization parameter and normalization. Neither setting the ionization parameter in `xillver` to be zero nor linking it to that in `relxillNS` could fit the line. The fit to the spectra with the model `tbabs*(diskbb+xillver +relxillNS+cutoffpl)` is reasonable, $\chi^2 = 946.0$ for 984 dof. However, the best-fitting ionization parameter is $3.77^{+0.17}_{-0.02}$, even higher than the one derived from `relxillNS`. This result is in conflict with our initial assumption of a distant reflection.

We then tried to see if the narrow line is the reemission from disk winds although without the sign of an absorption feature. We produced a grid of models with XSTAR again but adopting a `bbody` input spectrum with a blackbody temperature of 0.92 keV. We applied the same assumptions for the gas density and covering fraction as listed in Table 3 but changed the luminosity and the turbulent velocity to 3.9×10^{38} erg s^{-1} and 5000 km s^{-1}, respectively, based on the best-fitting parameters for the HXMT spectra. We replaced the component Gaussian with the precalculated grid and obtained the best fit with $\chi^2 = 942.1$ for 982 dof, the hydrogen equivalent column density, $10^{15} < N < 10^{22}$, the ionization parameter, $\log\xi = 4.41^{+0.24}_{-0.44}$, the blueshifted velocity, $v < 0.008c$, and the normalization, $N = 0.13^{+66.44}_{-0.08}$. Apparently, our data cannot constrain this complex photoionization model.

4. Discussion

After over three decades of quiescence, the black hole candidate EXO 1846–031 was again active. We studied its spectral properties in the hard intermediate and soft states in the

Table 4
Best-fitting Parameters of the HXMT Spectra of EXO 1846–031 with the Models `tbabs*(diskbb+Gaussian+relxill+cutoffpl)`, `tbabs*(diskbb +Gaussian+relxilllp+cutoffpl)` and `tbabs*(diskbb+Gaussian+relxillNS+cutoffpl)` in the Energy Bands 2–9 keV and 10–20 keV

Components		Insight-HXMT		
`tbabs`	N_H (10^{22} cm^{-2})	6.1 ± 0.1	6.1 ± 0.1	6.0 ± 0.1
`diskbb`	T_{dbb} (keV)	0.94 ± 0.01	0.94 ± 0.01	0.92 ± 0.01
	N_{dbb} ($R_{dbb}^2/D_{10}^2 \cos i$)	$1436.1^{+26.2}_{-52.5}$	$1439.6^{+1.1}_{-26.6}$	$1294.9^{+159.6}_{-205.4}$
`relxill(lp/NS)`	q_{in}	4.8 ± 0.8	$\cdots$	$3.9^{+0.9}_{-0.3}$
	h (R_g)	$\cdots$	<2	$\cdots$
	$\log n$ (cm^{-3})	$\cdots$	$\cdots$	19^f
	A_{Fe} ($A_{Fe\odot}$)	$1.5^{+1.0}_{-0.5}$	1.2 ± 0.2	$4.9^{10p}_{-1.9}$
	i (°)	$26.6^{+5.6}_{-13.1}$	$17.0^{+6.0}_{-9.5}$	<36.5
	a_*	0.998^f	0.998^f	0.998^f
	E_{cut} (keV)	500^f	500^f	500^f
	Refl_frac	-1^f	-1^f	-1^f
	R_{in}	3.4 ± 0.7 R_g	$3.9^{+0.9}_{-0.1}$ R_g	1^f R_{ISCO}
	$\log \xi$ (erg cm s^{-1})	$2.28^{+0.05}_{-0.54}$	$2.10^{+0.19}_{-0.04}$	$2.11^{+0.39}_{-0.10}$
	$N_{rel}/N_{relp}/N_{relns}$	0.06 ± 0.03	$9.7^{+10.1}_{-0.1}$	0.009 ± 0.003
`cutoffpl`	Γ	$3.02^{+0.09}_{-0.04}$	3.10 ± 0.12	1.97 ± 0.09
	N_{pl}	<0.14	<0.3	0.15 ± 0.05
`Gaussian`	E_{gau} (keV)	6.73 ± 0.03	6.74 ± 0.02	6.75 ± 0.03
	σ_{gau} (keV)	0.14 ± 0.04	0.11 ± 0.04	0.14 ± 0.05
	strength(10^{-3})	1.3 ± 0.2	1.1 ± 0.2	1.3 ± 0.4
`const`	LE	1^f	1^f	1^f
	ME	0.99 ± 0.03	0.98 ± 0.02	0.93 ± 0.03
χ^2/dof		941.2/982	944.1/981	944.0/983
	F_{dbb}	10.1 ± 0.1	10.1 ± 0.1	$8.4^{+0.9}_{-1.5}$
	$F_{rel}/F_{relp}/F_{relns}$	0.4 ± 0.1	0.4 ± 0.1	$1.6^{+1.5}_{-0.8}$
	F_{pl}	<0.09	<0.16	0.4 ± 0.1
	F_{tt}	10.5 ± 0.1	10.5 ± 0.1	10.4 ± 0.1

Note. The symbol p means that the parameter pegs at its limit; f means that the parameter is fixed during the fit. All the unabsorbed fluxes, F_{dbb}, F_{rel}, F_{relp}, F_{relns}, F_{pl}, and F_{tt}, are calculated in the energy band of $2-10$ keV in units of 10^{-9} erg cm^{-2}s^{-1}.

2019 outburst with NuSTAR and HXMT observations. A reflection component that becomes weaker from the intermediate to the soft state is present in both states. Fits with a reflection component yield an inclination angle of the accretion disk of $\sim 40°$ with respect to the line of sight. Besides that, a moderately broad absorption line has been observed at ~ 7.2 keV in the intermediate state but it disappears in the soft state, whereas a narrow emission is present at ~ 6.7 keV instead. In the following sections, we discuss the possible origin of the absorption and emission lines observed in EXO 1846–031.

4.1. Disk Wind in the Hard Intermediate State

There is evidence for an anticorrelation between jets and disk winds in LMXBs: jets are present in the hard state and disk winds are present in the soft state (e.g., Miller et al. 2006b, 2008). However, some studies show that jets and disk winds can coexist in the hard state (e.g., Homan et al. 2016; Gatuzz et al. 2020). Moreover, Homan et al. (2016) suggested that disk winds and jets do not need to be mutually exclusive in LMXBs when a source luminosity is higher than a few tens of percent of the Eddington luminosity.

Radio emissions of EXO 1846–031 have been detected with the VLA on August 1 (Miller-Jones et al. 2019) and MeerKAT on August 4 (Williams et al. 2019), respectively, indicating the presence of a jet. The NuSTAR observation, accompanied by an absorption line at ~ 7.2 keV, was performed on August 3, in between the radio detection. Therefore, the jet and disk wind are probably present simultaneously in EXO 1846–031. Adopting a distance of 8 kpc to the source (Miller-Jones et al. 2019) and a black hole mass of 3.24 $M_\odot$ (Strohmayer & Nicer Observatory Science Working Group 2020) gives an X-ray luminosity of ~ 0.1 L_{EDD} on August 3, consistent with the conclusion reported by Homan et al. (2016). Adopting a larger black hole mass, the corresponding X-ray luminosity would be lower than ~ 0.1 L_{EDD}, suggesting that for the coexistence of jets and disk winds, it is not essential that a source is brighter than tens of percent of the Eddington luminosity.

Thermally driven winds may occur when the launching radius is greater than the Compton radius, R_C, where the gravitational and thermal pressures are equal. Previous work suggests that such winds can even be driven from 0.1 R_C (Begelman et al. 1983; Woods et al. 1996). The Compton radius is given by

$$R_C = \frac{10^{10}}{T_{C,8}} \times \frac{M_{BH}}{M_\odot} \text{ cm}, \quad (1)$$

where $T_{C,8}$ is in units of 10^8 K. We calculate the Compton temperature via

$$T_{C,8} = \frac{h \int \nu E_\nu d\nu}{4k \int E_\nu d\nu}, \qquad (2)$$

where E_ν is the illuminating spectrum, h is the Planck constant, and k is the Boltzmann constant (Frank et al. 1985). When the spectrum is dominated by a cutoff power law in the intermediate state, we assume $E_\nu = Ke^{-\frac{h\nu}{E_{\rm cut}}}(h\nu)^{-\Gamma}$, where K is the normalization of `cutoffpl`. Adopting the best-fitting photon index and cutoff energy for either the low- or high-flux segment, this gives a Compton temperature of $T_{C,8} = 0.11 \pm 0.01$. Bringing this Compton temperature to Equation (1), we obtain $R_C = 29.5 \pm 0.01 \times 10^{10}$ cm when adopting a black hole mass of $3.24\,M_\odot$ from Strohmayer & Nicer Observatory Science Working Group (2020).

The launching radius is therefore about three orders of magnitude smaller than the Compton radius, $R_{\rm launch} = 0.001\,R_C$. If we considered a larger black hole mass for EXO 1846–031, the Compton radius would increase accordingly and hence the launching radius would be smaller, making it even less likely that such wind is driven by thermal expansion. Although by taking radiation pressure due to electron scattering into account, the launching radius could extend down to $0.01\,R_C$ (still one order of magnitude larger than our measurement), this requires a near-Eddington luminosity (Proga & Kallman 2002) or a sub-Eddington luminosity when the gas temperature is $< 10^5$ K (Proga 2007). As to line interaction, it is only effective for gas with low ionization (Proga et al. 2000). We therefore rule out the possibility of a radiation-driven wind in our case. This leaves magnetic forces as the only viable driving mechanism for the observed wind in EXO 1846–031.

Although disk winds have been largely detected in high-inclination systems, they have been detected in some low-inclination systems as well, for instance GX 340+0 (Miller et al. 2016), 1RXS J180408.9–342058 (Degenaar et al. 2016), and MAXI J1631–479 (Xu et al. 2020). Thermally driven winds are concentrated in the plane of the disk, and hence the line of sight is more likely to intercept the wind in high-inclination systems (e.g., Miller et al. 2006b; Tomaru et al. 2020). On the other hand, Chakravorty et al. (2016) suggest that magnetically driven winds can be observable at low inclination angles, which would match with our observations, although Chakravorty et al. (2016) also report that such winds can only be produced in the soft states. In conclusion, further studies are required to understand the observed winds/absorption lines in EXO 1846–031.

Draghis et al. (2020) applied the same reflection models `relxill(lp)` to fit the same NuSTAR observation of EXO 1846–031 as we did in this work. With a different model assumption, they derived different constraints of the system properties, e.g., a high spin parameter, $a_* = 0.995$–0.998, a high inclination angle of the accretion disk, $i \approx 73°$, and a subsolar iron abundance, $A_{\rm Fe} = 0.58$–0.87. We reexamined the NuSTAR data to explore why we obtained such divergent results with the model `tbabs*(diskbb+relxill)`. The absorption-line model is removed to avoid the effect of the degeneracy between `relxill` and `gabs`. The result shows that the reflection fraction (refl_frac in `relxill`) played a key role here. If we freeze the reflection fraction to be 1, as Draghis et al. (2020) assumed in their work, let the spin parameter free, and keep the other assumption

for `relxill` as described in Section 3.1.1 in the fit, we would obtain a spin parameter, $a_* = 0.96 \pm 0.02$, a much higher inclination angle, $i = 84.4 \pm 0°.2$, and a subsolar iron abundance, $A_{\rm Fe} = 0.67 \pm 0.03$, with a worse fit $\Delta\chi^2 = 112.3$ for 1 dof more. Because we split the NuSTAR observation into two segments, if we use the same assumption as in Draghis et al. (2020), we would have more free parameters in the model and thus cannot constrain parameters as well as they did. Because the only thing we want to show here is that the best-fitting parameters Draghis et al. (2020) obtained are strongly dependent on the value of the reflection fraction, we did not conduct this test further.

4.2. Illuminating Source in the Soft State

We conducted a spectral analysis of the observations of EXO 1846–031 in both the intermediate and soft states. For the spectra in the intermediate state, we fitted the continuum with the same model but fitted the reflection spectrum with either `relxill` or `relxilllp`. The best-fitting parameters are consistent within the two models and are in good agreement with the spectral state. However, the fit to the spectra in the soft state is debatable. As described in Section 3.1.2, we have fitted the HXMT spectra with three versions of the reflection models, `relxill`, `relxilllp`, and `relxillNS`, which assume different types and geometries of its illuminating source.

In the fits with either `relxill` or `relxilllp`, the hard component, which is the required illuminating source for both models, is negligible. We define the reflection strength as a ratio of the reflected to the incident flux in the 10–20 keV band, where we see a Compton hump in the HXMT observation. The reflection strength is 2×10^8 for `relxill` and 5×10^8 for `relxilllp`, both of which are unrealistically high for any configuration.

Moreover, the best-fitting photon index derived from `relxill` or `relxilllp` is around 3. Such a high value of the photon index is normally observed in a "very high" state (VHS) or "steep power-law" (SPL) state in which the spectrum is characterized by a strong power-law component (Miyamoto et al. 1993; van der Klis 2004). This is in conflict with the fact that the soft component `diskbb` contributes over 96% of the total flux in this observation when fitting the reflection spectrum with either `relxill` or `relxilllp`. If we freeze Γ at 2, the fit worsens by $\Delta\chi^2 = 24.6$; meanwhile, the best-fitting inclination angle pegs at 3°, not consistent with the value derived from the fit to the NuSTAR spectra. Overall, both models are very doubtful for explaining the reflection features present in the HXMT observation.

In terms of `relxillNS`, the model fits the data well, and the derived iron abundance and the inclination angle of the accretion disk are in accordance with the ones derived from the fit to the NuSTAR spectrum in the intermediate state. These results leave us the possibility that we may observe another case of the disk self-irradiating reflection spectrum in a BHXB (the first one is reported by Connors et al. 2020). When the inner radius of the accretion disk reaches the ISCO, the gravity of the central compact source is strong enough to bend the light from the disk on itself. To explore if this is a physically viable theory for EXO 1846–031, we calculate the fraction of photons returning to the disk based on general relativistic ray-tracing simulations (see more details in Connors et al. 2020). Using the code developed by Yang & Wang (2013) and adopting a standard prescription for the disk emission with zero-torque condition (Shakura & Sunyaev 1973; Poutanen et al. 2007), we

estimated the fraction as a function of spin. Assuming a spin of 0.998, the estimated fraction is about 18%, in good agreement with the observed value, i.e., $F_{\text{relns}}/F_{\text{tt}} = 18\%$ (see Table 4). This result suggests that disk self-irradiation could be the origin of the observed reflection feature in EXO 1846–031. However, it should be kept in mind that this is just a rough estimate of the photons returning to the disk, which could be very different from what the disk sees in reality when taking general relativity energy shifts into account. Further exploration is beyond the scope of this work. More details will be presented in T. Dauser & J. García (2020, in preparation).

4.3. Origin of the Narrow Emission Line in the Soft State

Disk winds, identified by absorption lines, have been commonly observed in LMXBs in the soft state (e.g., Miller et al. 2008; Neilsen & Lee 2009; Miller et al. 2015). However, we only observed absorption lines in the intermediate rather than the soft state in EXO 1846–031. As we mentioned in Section 3.1.2, a narrow emission line at ∼6.7 keV is present on top of the reflection component regardless of the choice of reflection model. We have tested two possibilities for its origin, a distant reflection or reemission from disk winds. The former has been ruled out because, for the same electron density, the fit of a distant reflection yields an even higher ionization parameter than the near one. The latter cannot be confirmed either as the overall model is too complex to be constrained by the HXMT data.

Díaz Trigo et al. (2014) suggested another possible origin for a narrow emission line present in BHXBs. By analyzing six XMM-Newton observations of 4U 1630–47, Díaz Trigo et al. (2014) interpreted the disappearance of a disk wind, i.e., the absence of an absorption line, as a consequence of strong ionization of the wind when 4U 1630–47 transited from the high soft to the VHS/SPL and attributed a narrow emission line above 7 keV to arise in an optically thin jet while 4U 1630–46 was in the VHS/SPL. Although without including any radio observation in our work it is hard to tell the presence of jets in EXO 1846–031 in the soft state, the observed hard emission seems too weak to be responsible for that.

If the narrow line is not from disk winds, then the disk winds observed in the intermediate state disappeared in the soft state. Because the input source in the soft state is much brighter than the one in the intermediate state, the disk wind could become "transparent" due to a strong ionization as Díaz Trigo et al. (2014) suggested. Overall, observations with higher spectral resolution are required to examine this result.

5. Conclusion

We analyzed NuSTAR and HXMT observations of EXO 1846–031 in the hard intermediate and soft states. By fitting a reflection component, we obtained an inclination angle of ∼40° with respect to the line of sight. Our fit of the absorption line at ∼7.2 keV indicates a highly ionized fast outflowing disk wind with an ionization parameter, $\log \xi > 5.7$, and a velocity up to 0.06c. The quasi-simultaneous radio emissions reported in the literature suggest jets and disk winds probably coexist in EXO 1846–031. With the modest spectral resolution of NuSTAR, the observed wind in the high-flux segment appears to be magnetic driven.

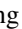A weak reflection component has been detected in the HXMT observation in the soft state. We tried to fit it with the different versions of reflection models, `relxillNS`, `relxill`, and `relxilllp`, and all of them returned a reasonable fit. For the fit with `relxillNS`, this model describes the reflection spectrum well, and the obtained inclination angle and the iron abundance are consistent with the ones derived in the intermediate state, implying a possible detection of self-irradiating disk reflection. Assuming a standard accretion disk with zero-torque condition (Shakura & Sunyaev 1973), Connors et al. (2020) found that ∼5% of the photons could return to the disk when a spin of 0.5 is adopted, which is well matched with their observation. In the case of EXO 1846–031, the fraction of the reflected flux with respect to the direct emission is ∼18%, over three times larger than their detection. However, using the same assumption and meanwhile adopting a spin of 0.998, the estimate of returning photons is also three times larger than that in Connors et al. (2020). Overall, this result states that disk self-irradiation is able to produce the reflection features observed in EXO 1846–031 in the soft state. As to the latter two models, both of them require a very large photon index and an extremely high reflection strength, making both scenarios less convincing. The origin of the narrow emission line at ∼6.7 keV is still debatable. X-ray data with the higher spectral resolution, e.g., Chandra and X-Ray Imaging and Spectroscopy Mission (XRISM; Tashiro et al. 2018; XRISM Science Team 2020), are required to further investigate this.

ORCID iDs

Javier A. García https://orcid.org/0000-0003-3828-2448
L. Tao https://orcid.org/0000-0002-2705-4338

Diego Altamirano ⓘ https://orcid.org/0000-0002-3422-0074
S. N. Zhang ⓘ https://orcid.org/0000-0001-5586-1017
M. Y. Ge ⓘ https://orcid.org/0000-0002-2749-6638
L. Zhang ⓘ https://orcid.org/0000-0003-4498-9925
J. L. Qu ⓘ https://orcid.org/0000-0002-9796-2585
F. J. Lu ⓘ https://orcid.org/0000-0003-3248-6087
Y. Chen ⓘ https://orcid.org/0000-0001-9834-2196
Q. C. Bu ⓘ https://orcid.org/0000-0001-5238-3988
S. M. Jia ⓘ https://orcid.org/0000-0002-5203-8321
L. D. Kong ⓘ https://orcid.org/0000-0003-3188-9079
B. Li ⓘ https://orcid.org/0000-0002-0238-834X
C. K. Li ⓘ https://orcid.org/0000-0001-5798-4491
G. Li ⓘ https://orcid.org/0000-0001-5067-1599
X. F. Li ⓘ https://orcid.org/0000-0002-2793-9857
Q. Luo ⓘ https://orcid.org/0000-0003-1853-7810
Q. Q. Yin ⓘ https://orcid.org/0000-0001-7580-1513

References

Altamirano, D., & Méndez, M. 2015, MNRAS, 449, 4027
Arnaud, K. A. 1996, in ASP Conf. Ser. 101, Astronomical Data Analysis Software and Systems V, ed. G. H. Jacoby & J. Barnes (San Francisco, CA: ASP), 17
Begelman, M. C., McKee, C. F., & Shields, G. A. 1983, ApJ, 271, 70
Belloni, T., Klein-Wolt, M., Méndez, M., van der Klis, M., & van Paradijs, J. 2000, A&A, 355, 271
Belloni, T. M. 2010, in The Jet Paradigm: From Microquasars to Quasars, Lecture Notes in Physics, Vol. 794, ed. T. Belloni (Berlin: Springer), 53
Cackett, E. M., Miller, J. M., Ballantyne, D. R., et al. 2010, ApJ, 720, 205
Cao, X., Jiang, W., Meng, B., et al. 2020, SCPMA, 63, 249504
Cash, W. 1979, ApJ, 228, 939
Chakravorty, S., Petrucci, P. O., Ferreira, J., et al. 2016, A&A, 589, A119
Chen, W., Shrader, C. R., & Livio, M. 1997, ApJ, 491, 312
Chen, Y., Cui, W., Li, W., et al. 2020, SCPMA, 63, 249505
Connors, R. M. T., García, J. A., Dauser, T., et al. 2020, ApJ, 892, 47
Dauser, T., Garcia, J., Parker, M. L., Fabian, A. C., & Wilms, J. 2014, MNRAS, 444, L100
Dauser, T., García, J., Walton, D. J., et al. 2016, A&A, 590, A76
Dauser, T., Garcia, J., Wilms, J., et al. 2013, MNRAS, 430, 1694
Degenaar, N., Altamirano, D., Parker, M., et al. 2016, MNRAS, 461, 4049
Díaz Trigo, M., Migliari, S., Miller-Jones, J. C. A., & Guainazzi, M. 2014, A&A, 571, A76
Draghis, P. A., Miller, J. M., Cackett, E. M., et al. 2020, ApJ, 900, 78
Fabian, A. C., Parker, M. L., Wilkins, D. R., et al. 2014, MNRAS, 439, 2307
Frank, J., King, A., & Raine, D. J. 2002, Accretion Power in Astrophysics: Third Edition (Cambridge: Cambridge Univ. Press)
Frank, J., King, A. R., & Raine, D. J. 1985, Accretion Power in Astrophysics (Cambridge: Cambridge Univ. Press)
García, J., Dauser, T., Lohfink, A., et al. 2014, ApJ, 782, 76
García, J. A., Steiner, J. F., McClintock, J. E., et al. 2015, ApJ, 813, 84
Gatuzz, E., Díaz Trigo, M., Miller-Jones, J. C. A., & Migliari, S. 2020, MNRAS, 491, 4857
Gehrels, N., Chincarini, G., Giommi, P., et al. 2004, ApJ, 611, 1005
George, I. M., & Fabian, A. C. 1991, MNRAS, 249, 352
Guo, C.-C., Liao, J.-Y., Zhang, S., et al. 2020, JHEAp, 27, 44
Harrison, F. A., Craig, W. W., Christensen, F. E., et al. 2013, ApJ, 770, 103
Homan, J., Neilsen, J., Allen, J. L., et al. 2016, ApJL, 830, L5
Janiuk, A., Grzedzielski, M., Capitanio, F., & Bianchi, S. 2015, A&A, 574, A92
Kallman, T., & Bautista, M. 2001, ApJS, 133, 221
Laor, A. 1991, ApJ, 376, 90

Liao, J.-Y., Zhang, S., Chen, Y., et al. 2020, JHEAp, 27, 24
Lightman, A. P., & White, T. R. 1988, ApJ, 335, 57
Liu, H.-X., Huang, Y., Xiao, G.-C., et al. 2020, arXiv:2009.10956
Markoff, S., Nowak, M. A., & Wilms, J. 2005, ApJ, 635, 1203
Méndez, M., & van der Klis, M. 1997, ApJ, 479, 926
Miller, J. M. 2007, ARA&A, 45, 441
Miller, J. M., Fabian, A. C., Kaastra, J., et al. 2015, ApJ, 814, 87
Miller, J. M., Raymond, J., Cackett, E., Grinberg, V., & Nowak, M. 2016, ApJL, 822, L18
Miller, J. M., Raymond, J., Fabian, A., et al. 2006a, Natur, 441, 953
Miller, J. M., Raymond, J., Fabian, A. C., et al. 2012, ApJL, 759, L6
Miller, J. M., Raymond, J., Homan, J., et al. 2006b, ApJ, 646, 394
Miller, J. M., Raymond, J., Reynolds, C. S., et al. 2008, ApJ, 680, 1359
Miller, J. M., Zoghbi, A., Gandhi, P., & Paice, J. 2019, ATel, 13012, 1
Miller-Jones, J., Russell, T., Sivakoff, G., & Tetarenko, A. 2019, ATel, 12977, 1
Miyamoto, S., Iga, S., Kitamoto, S., & Kamado, Y. 1993, ApJL, 403, L39
Miyamoto, S., Kimura, K., Kitamoto, S., Dotani, T., & Ebisawa, K. 1991, ApJ, 383, 784
Muñoz-Darias, T., Motta, S., & Belloni, T. M. 2011, MNRAS, 410, 679
Neilsen, J., & Lee, J. C. 2009, Natur, 458, 481
Parmar, A. N., Angelini, L., Roche, P., & White, N. E. 1993, A&A, 279, 179
Ponti, G., Fender, R. P., Begelman, M. C., et al. 2012, MNRAS, 422, L11
Poutanen, J., & Fabian, A. C. 1999, MNRAS, 306, L31
Poutanen, J., Lipunova, G., Fabrika, S., Butkevich, A. G., & Abolmasov, P. 2007, MNRAS, 377, 1187
Proga, D. 2007, in ASP Conf. Ser. 373, The Central Engine of Active Galactic Nuclei, ed. L. C. Ho & J. W. Wang (San Francisco, CA: ASP), 267
Proga, D., & Kallman, T. R. 2002, ApJ, 565, 455
Proga, D., Stone, J. M., & Kallman, T. R. 2000, ApJ, 543, 686
Remillard, R. A., & McClintock, J. E. 2006, ARA&A, 44, 49
Ross, R. R., & Fabian, A. C. 2005, MNRAS, 358, 211
Shakura, N. I., & Sunyaev, R. A. 1973, A&A, 500, 33
Strohmayer, T. E. & Nicer Observatory Science Working Group 2020, AAS Meeting, 235, 159.02
Tanaka, Y., & Shibazaki, N. 1996, ARA&A, 34, 607
Tao, L., Tomsick, J. A., Walton, D. J., et al. 2015, ApJ, 811, 51
Tarter, C. B., Tucker, W. H., & Salpeter, E. E. 1969, ApJ, 156, 943
Tashiro, M., Maejima, H., Toda, K., et al. 2018, Proc. SPIE, 10699, 1069922
Tomaru, R., Done, C., Ohsuga, K., Nomura, M., & Takahashi, T. 2019, MNRAS, 490, 3098
Tomaru, R., Done, C., Ohsuga, K., Odaka, H., & Takahashi, T. 2020, MNRAS, 497, 4970
Tomsick, J. A., & Kaaret, P. 2000, ApJ, 537, 448
Trueba, N., Miller, J. M., Kaastra, J., et al. 2019, ApJ, 886, 104
Ueda, Y., Yamaoka, K., & Remillard, R. 2009, ApJ, 695, 888
Uttley, P., Cackett, E. M., Fabian, A. C., Kara, E., & Wilkins, D. R. 2014, A&ARv, 22, 72
Uttley, P., McHardy, I. M., & Vaughan, S. 2005, MNRAS, 359, 345
van der Klis, M. 1995, in The Lives of the Neutron Stars, NATO ASI Ser. C, Vol. 450, ed. M. A. Alpar, U. Kiziloglu, & J. van Paradijs (Dordrecht: Kluwer Academic), 301
van der Klis, M. 2004, arXiv:astro-ph/0410551
Wang, Y., Ji, L., Zhang, S. N., et al. 2020, ApJ, 896, 33
Wang, Y., Méndez, M., Altamirano, D., et al. 2018, MNRAS, 478, 4837
Wang, Y., Méndez, M., Altamirano, D., et al. 2019, MNRAS, 484, 3004
Williams, D., Fender, R., Woudt, P., & Miller-Jones, J. 2019, ATel, 12992, 1
Wilms, J., Allen, A., & McCray, R. 2000, ApJ, 542, 914
Woods, D. T., Klein, R. I., Castor, J. I., McKee, C. F., & Bell, J. B. 1996, ApJ, 461, 767
XRISM Science Team 2020, arXiv:2003.04962
Xu, Y., Harrison, F. A., Tomsick, J. A., et al. 2020, ApJ, 893, 30
Yang, X. L., & Wang, J. C. 2013, AcASn, 54, 493
Yang, Y.-J., Xiao, G., Soria, R., et al. 2019, ATel, 13037, 1
Zhang, S.-N., Li, T., Lu, F., et al. 2020, SCPMA, 63, 249502